AERODYNAMIC AND STRUCTURAL EVALUATION OF AN SMA SLAT-COVE FILLER USING COMPUTATIONAL AND EXPERIMENTAL TOOLS AT MODEL SCALE

William Scholten
Ryan Patterson
Makiah Eustice
Department of Aerospace Engineering
Texas A&M University
College Station, TX 77843-3409

Sebastian Cook
Darren Hartl
Thomas Strganac
Department of Aerospace Engineering
Texas A&M University
College Station, TX 77843-3409

Travis Turner
Structural Acoustics Branch
NASA Langley Research Center
Hampton, VA 23681-2199

ABSTRACT

Transport class aircraft produce a significant amount of airframe noise during approach and landing due to exposed geometric discontinuities that are hidden during cruise. The leading-edge slat is a primary contributor to this noise. In previous work, use of a slat-cove filler (SCF) has proven to reduce airframe noise by filling the cove aft of the slat, eliminating the circulation region within the cove. The goal of this work is to extend and improve upon past experimental and computational efforts on the evaluation of a scaled high-lift wing with a superelastic shape memory alloy (SMA) SCF. Recent turbulence measurements of the Texas A&M University 3ft-by-4ft wind tunnel allow for more accurate representation of the flow through the test section in computational fluid dynamics (CFD) analysis. The finite volume models used in CFD analysis are coupled to structural finite element models using a framework compatible with an SMA constitutive model and significant deformation, enabling fluid-structure interaction (FSI) analysis of the SCF. Both fully-deployed and retraction/deployment cases are considered. The displacement of the SCF on the experimental model is measured at various stages of retraction/deployment using a laser displacement sensor and digital image correlation system. Due to a lack of structural stiffness in the 3D-printed plastic slat during retraction and SCF stowage, a rigid steel slat is incorporated into the physical model and preliminary wind tunnel tests are conducted at multiple angles of attack in both retracted and deployed configurations.

1 Introduction

During approach and landing (low-speed, low altitude maneuvers), transport aircraft improve flight characteristics by deploying high-lift devices, such as the leading-edge slat and trailing-edge flap. These devices are flush against the main wing during cruise for reduced drag, but when deployed, the high-lift system exposes edges, coves, and other geometric discontinuities to the airflow that result in the production of airframe noise. Noise produced by aircraft near airports is a growing concern for the aerospace community due to environmental impacts in surrounding residential areas. The slat-cove filler (SCF), a concept tested both experimentally and computationally [1–4], redirects flow along an acoustically advantageous path by filling the cove aft of the leading-edge slat.

Due to significant deformation of the SCF during slat actuation between retracted and deployed configurations, shape memory alloys (SMAs) are incorporated into the design. SMAs, a type of active material, are considered in morphing aerospace designs due to high energy density, large recoverable deformation, and system complexity reduction [5]. Specifically in this work, superelastic SMAs are used, which exhibit a phase transformation under sufficient mechanical loading.

Initial work on the SMA SCF concept began with development of physical benchtop models (both monolithic and multielement SCF designs) [6]. Computational finite element models were then developed for the SMA SCF and design optimization was conducted, considering minimization of actuation loading

1

required to stow the SMA SCF during slat retraction. The optimization was subject to constraints on maximum stress, deflection from aerodynamic forces, and ability to redeploy the SCF when the slat deploys [7, 8]. Alternative means of reducing actuation force were considered such as the addition of auxiliary actuators to rotate the SCF prior to slat retraction [9], and work continues on composite alternatives to the SMA SCF [10]. Work then shifted toward the development and testing of a wind tunnel scale high-lift wing with an installed SMA SCF and movable slats/flaps. Wind tunnel tests consisted of measuring lift and drag of the wing and the pressure distribution on the surface of the wing at various angles of attack and configurations. Concurrently, computational fluid dynamics (CFD) and fluid-structure interaction (FSI) models were created and results from those models were compared to wind tunnel data [11, 12].

The goal of this work is improvement and extension of past efforts that focused on using computational and experimental tools to understand SMA SCF behavior in flow. Both the scaled wind tunnel model and computational models are based on a freestream-aligned, spanwise section of the Boeing-NASA Common Research Model (CRM) [13]. New metrologies are added to the wind tunnel that allow for measurement of SCF displacement while new computational models are developed that allow for FSI analysis of the SCF during retraction and deployment. Section 2 summarizes the concept of the SMA SCF. Section 3 describes the computational structure and fluid models. Section 4 discusses the FSI framework, remeshing scheme for large SCF deformation, and presents results for multiple load cases. Section 5 provides details on the wind tunnel model, results from structural and aerodynamic testing and comparisons with computational models. The work is summarized and future efforts are presented in Section 6.

2 SCF Concept

As mentioned previously, unsteady flow in and around the leading-edge slat-cove is a source of airframe noise during approach and landing phases of flight. A typical flow field near the slat during landing is shown in Fig. 1(a). Following bifurcation of the flow at the slat stagnation point, flow along the lower surface of the slat separates at the forward edge of the cove (a geometric discontinuity) creating a shear layer that reattaches near the trailing edge of the slat. A flow circulation region is developed between the shear layer and walls of the slat-cove, leading to significant airframe noise production.

The deployed SCF reduces airframe noise produced by the slat through the elimination of the slat-cove and redirecting of flow along a path that substantially reduces the unsteadiness (as shown in Fig. 1(b)). As the SCF guides the flow, it is subjected to aerodynamic loading and must maintain its shape (i.e., have sufficient stiffness). However, as the slat is retracted into a stowed position, the SCF must also be compliant to deform around the

(a) Unmodified slat.

(b) Slat with SCF.
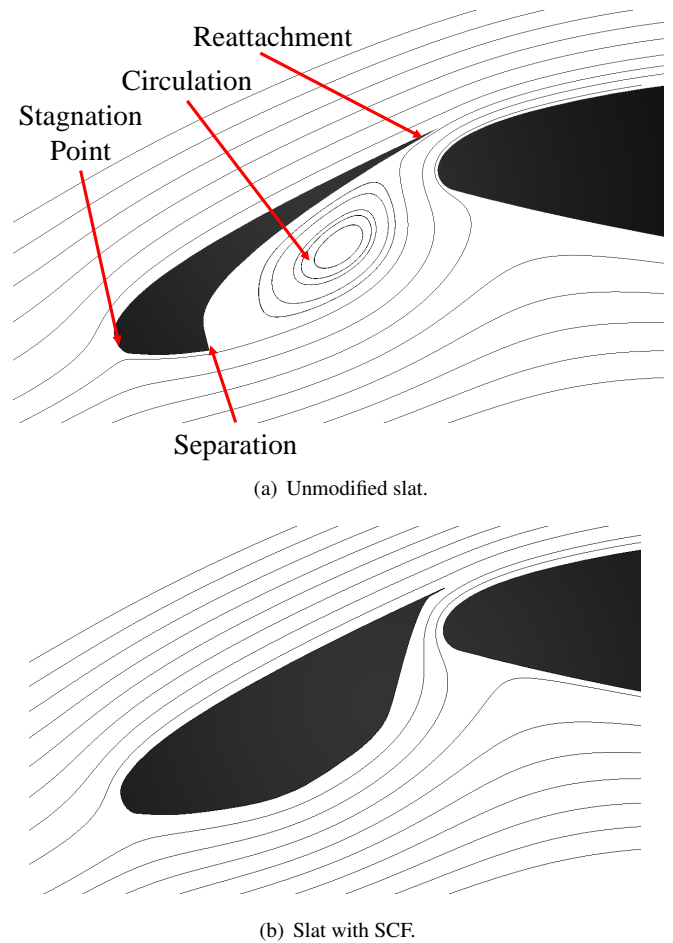
FIGURE 1. Streamlines of flow in the vicinity of the leading-edge slat for the CRM airfoil (from [11]).

main wing without significant additional actuation force and allow the retracted slat to be flush against the main wing. Strain due to reconfiguration of the SCF during stowage (approximately 2-5%) prevents the use of traditional aerospace materials in the SCF design for typical applications [6]. This strain, in addition to the conflicting requirements of stiffness when deployed and compliance when retracted, led to the incorporation of superelastic SMAs, a type of active material. With sufficient loading, such as local stress concentrations in the SCF during retraction, superelastic SMAs undergo a solid-state transformation from austenite to martensite enabling large recoverable deformation. When unloaded, such as when the slat is deployed, the SMA material returns to its undeformed configuration through reverse transformation.

2

3 Computational Models

In this section, a description of the computational and fluid models is provided. Additional changes to the fluid model for compatibility with FSI analysis are discussed. As previously mentioned, the SCF profile considered in this work is for the high-lift variant of the Boeing-NASA CRM, an open-source geometry of a transport-class aircraft developed for the purpose of validating CFD results and evaluating new technologies [13, 14]. The base geometry of both computational and experimental models is from a 6.25% scale 2D section of the CRM at the midspan of the outboard slat aligned with the freestream-direction, which has a stowed chord of 0.3216 m.

3.1 Finite Element Structural Models

The finite element structural model, shown in Fig. 2(a) is created using Abaqus [15], a commercial finite element suite. All components in the model are one element wide in the spanwise direction with a length of 1.0 mm. The entire outer mold line (OML) of the slat and SCF is modeled as a single deformable shell (see Fig. 2(b)) for the purpose of improving the FSI implementation by linking the structure and fluid models with the surface of a single closed volume (the slat/SCF). The negative offset of the slat cusp, indicated by the blue outline in the inset of Fig. 2(a), was introduced in the computational model to assist in the accommodation of FSI analysis, specifically the snapping of the hinge during deployment and retraction. Rigid bodies in the model include the hinge, main wing leading-edge, and a rigid slat that is connected via a tie constraint to the slat OML of the deformable slat/SCF. Applying a rotational displacement about the rigid slat reference point simulates slat retraction and deployment, which is a circular arc in the physical model. A rotation of 0.44 rad fully retracts the slat from the deployed configuration. The potential for transient dynamic behavior of the SCF during slat articulation, e.g., snap-through, or due to aerodynamic fluctuating pressures requires the use of an implicit dynamic solver (a *Dynamic Implicit step in Abaqus).

The thickness of the SCF portion of the OML shell is set to 0.0762 mm (0.003 in), which matches the 6.25% scaled experimental prototype of the SCF employed on the wind-tunnel model. The SMA SCF portion has a mesh of 262 general shell elements (type S4R). An infinitely-long SCF in the spanwise direction is simulated through the application of symmetry conditions on the edges of the OML shell aligned with the X-Y plane. The length (2.16 mm) of the SCF-hinge arm (projection of the hinge onto the SCF) and placement of the hinge (1.13 mm from cove wall) are based on results from an optimization study (similar to previous work [8]) with an objective of minimizing the actuation force components (horizontal and vertical) required to retract the slat/SCF. To model contact between the SCF and the various parts, surface-to-surface contact is implemented. A linear penetration penalty law is utilized to prevent surface-surface
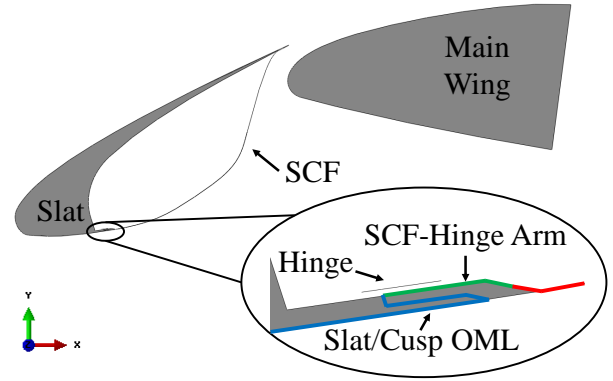

(a) Overall Assembly
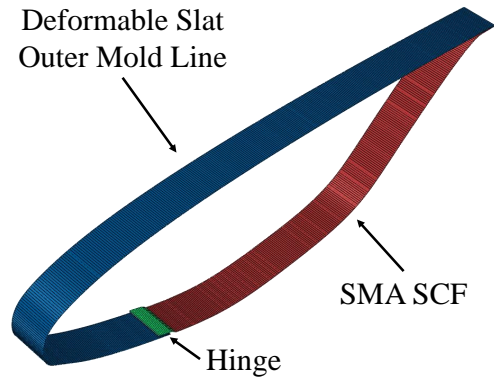
(b) Mesh of Slat/SCF OML.

FIGURE 2. Structural FEA model of 2.5D SMA SCF assembly.

penetration in the normal direction while contact in the tangential direction is modeled with a friction coefficient of 0.42, which was measured experimentally [12].

The constitutive model developed by Lagoudas, Hartl, and coworkers [16] is used in this work to capture the thermomechanical behavior of SMAs. In Abaqus, this constitutive model is implemented as a user material (UMAT). Previous work [12] included tensile tests (per ASTM standards [17]) of SMA dogbone specimens created from the same raw material as the SMA SCF. The stress-strain response of the material at different temperatures was used to calibrate the material properties for the UMAT (see Table 1). Figure 3 shows the calibrated output from the UMAT superimposed onto experimental data.
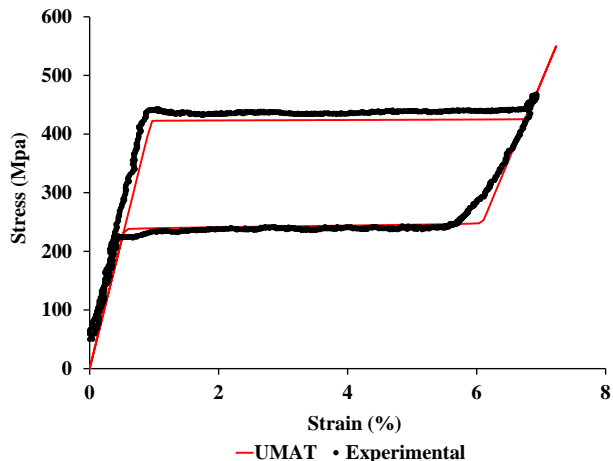
FIGURE 3. Comparison of hysteris loop from calibrated UMAT and experimental data [12].

3.2 Computational Fluid Dynamics Model

CFD analysis is conducted with SC/Tetra, a thermo-fluid unstructured mesh solver developed by Cradle [18], which incorporates finite volume methods to solve both laminar and turbulent flows. Features that make SC/Tetra viable for use in this work include: 1) a built-in link to the Abaqus Co-Simulation Engine and 2) overset meshes that enable the modeling of complex relative translations and rotations of parts, and 3) deformable meshes that account for deformation such as the outer mold line of the slat/SCF during articulation. The CFD models used in this work include both the wing in its various configurations and the test section (2.74 m in length) of the Texas A&M University 3 ft-by-4 ft (0.91 m-by-1.22 m) wind tunnel. A CFD model of the wing in the deployed configuration and treated with the SCF, termed the SCF-treated deployed configuration, in the test section of the wind tunnel is shown in Fig. 4. Geometry of the wing matches the physical wind tunnel model to the greatest extent possible. The wing configurations of interest include the fully deployed slat/flap with no SCF (untreated deployed), retracted, and fully deployed slat/flap with the SCF (SCF-treated deployed). Aspects of the modeled test section include the inlet, outlet, bottom (floor) wall, and top (ceiling) wall. Since the wind tunnel model spans the entire width of the test section, the CFD model is one element wide in the spanwise direction (i.e., neglecting spanwise effects), significantly reducing the computational runtime for both CFD and FSI analysis.

For ease of mesh specification, the model consists of three closed volume regions: 1) outer, 2) middle, and 3) inner, the latter of which includes the solid closed volumes of the wing. The boundary of the inner volume region is based on an offset from the wing outer mold line equal to 10% of the retracted chord. The middle volume region is defined as a 1-chord-by-2-chord box

TABLE 1. SMA material properties from [12].

PROPERTY	VALUE
(Elastic Properties)	
E_A, E_M	44.2 GPa, 26.4 GPa
$\nu_A = \nu_M$	0.33
(Phase Diagram Properties)	
M_s, M_f	236.9 K, 236.5 K
A_s, A_f	266.6 K, 268.1 K
$C^A = C^M$	7.1 MPa/K, 7.7 MPa/K
(Transformation Strain Properties)	
$H = H_v$	5.15%
(Smooth Hardening Properties)	
n_1, n_2, n_3, n_4	0.5
(Other Properties)	
ρ	6480 kg/m^3
$\alpha_M = \alpha_A$	0
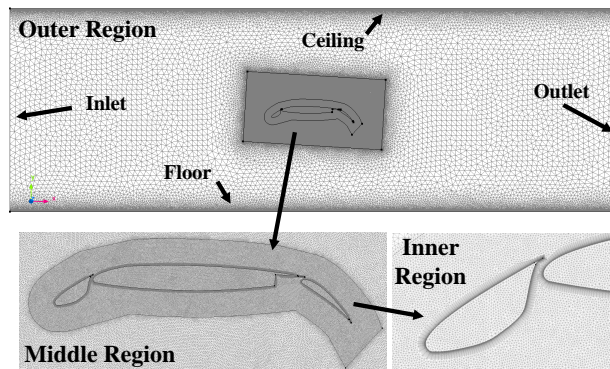
FIGURE 4. CFD model of CRM wing with the SCF-treated deployed configuration in the test section.

centered about the midchord of the retracted configuration. The remaining domain of the model is the outer volume region. Each volume region is assigned an element size. The element size in the outer volume region is 25.6 mm while a size of 0.8 mm is assigned in the inner volume region. These element size selections maintain accuracy of the analysis while reducing computational cost. Note that the element size along the surfaces of the test

section floor and ceiling in the outer volume region are refined to the same level as the inner volume region in order to capture the viscous effects and boundary layer properly. Layers of hexahedron elements are inserted along the surfaces of the wing and test section floor/ceiling to improve the fidelity of the boundary layer. Element sizes of the model and parameters for the hexahedron layers are based on mesh studies that examine how lift and drag are affected by changes in the mesh.

Boundary conditions applied to the CFD model include 1) freestream flow (both velocity and turbulence properties) at the inlet, 2) zero static pressure (i.e., no pressure gradient) at the outlet, and 3) smooth, no-slip/penetration walls on the surface of the floor, ceiling, and wing. For all flow analysis (both CFD and FSI), the fluid is incompressible air with viscosity of 1.83×10^5 Pa-s and density of 1.206 kg/m^3. Turbulent aspects of the flow, such as separation on the high-lift devices and recirculation of flow in the slat-cove, are modeled with a Shear-Stress Transport (SST) $k - \omega$ turbulence model [19], which is a two-equation turbulence model that utilizes zonal treatment to transition between flow near the wall and far-field flow. At the inlet, turbulent kinetic energy k and turbulent dissipation rate ε are specified. Approximately laminar flow at the inlet is modeled when k and ε are 0.0001 m^2/s^2 and 0.0001 m^2/s^3, respectively. Accurate values of both properties are required to properly model the flow through the test section. Turbulent kinetic energy can be experimentally determined using a hot wire anemometer, which measures velocity to a high precision at a single point in the flow. The fluctuation in velocity, represented as the root-mean square of the velocity (U_{RMS}), is directly related to the turbulent kinetic energy through the following equation

$$k = \frac{3}{2}(U_{RMS})^2. \tag{3.1}$$

The turbulent dissipation rate is estimated using the relation,

$$\varepsilon = \frac{0.09^{\frac{3}{4}} \cdot k^{\frac{3}{2}}}{0.07D}, \tag{3.2}$$

where D is the equivalent diameter of the rectangular inlet. Preliminary velocity measurements were taken over a single plane in an empty test section of the wind tunnel using a hot wire anemometer mounted to a newly, renovated three degree-of-freedom traversing system. In the vicinity of where the wing is to be mounted, the turbulent kinetic energy at flow speed of 15 m/s was measured to be 0.68 m^2/s^2 (4.5% turbulent) with a corresponding dissipation rate of 1.15 m^2/s^3 while the turbulent energy and dissipation rate were 0.57 m^2/s^2 and 0.68 m^2/s^2 at a flow speed of 20 m/s (3.1% turbulent).

4 FSI Model and Analysis

This section details work on the FSI analysis of the SMA SCF. Changes to the fluid model for accommodating FSI analysis are provided followed by a brief summary of the framework (more information can be found in [12]) and presentation of the remeshing scheme. Results for two load cases are provided: 1) fixed, fully deployed, and 2) retraction/deployment of the slat/SCF.

4.1 Changes to the Fluid Model

During slat retraction, the SMA SCF stows between the main wing and the slat, leading to a significant reduction of fluid volume in the slat cove, while during slat deployment, there is a large increase in fluid volume as the SMA SCF returns to its original configuration. Both volume changes can lead to elements with zero volume through compressing and/or stretching, resulting in numerical instabilities during the analysis. The volume changes are accommodated through the use of overset meshes, which allow deformable, movable slave meshes to coincide in the same location as a fixed master mesh. Interpolation transmits flow data between the outer boundary of the slave meshes and master mesh.

Implementation of overset meshes for the SCF problem is shown in Fig. 5. For this work, the test section and main wing are incorporated into the master mesh as neither component will move during FSI analysis, while the high lift devices are slave meshes. Previous work separated the SMA SCF and slat into two slave meshes, but interaction between the two slave meshes led to difficulties in running FSI analysis. In this work, the slat and SCF are included in a single slave mesh that reduces the complexity associated with building the FSI model. Additionally, the mesh is refined in the vicinity of the high lift devices. Movement of the slat/SCF is dictated by the structural model (see following section) while movement of the flap is controlled by SC/Tetra. The flap is not controlled in the structural model since only the forward part of the wing is modeled in the structure. User-defined functions in SC/Tetra apply prescribed translations and rotations to the flap based on kinematic relations of the physical model (i.e., the flap in the computational analysis moves in the same way as the flap in the physical model). Both the flap and slat are articulated at the same rate.

During FSI analysis attempts considering slat/SCF retraction via preliminary models, fatal numerical instabilities were introduced when the SCF came into contact with the surface of the wing due to elimination of fluid between the two bodies. Introduction of an artificial, negative offset of 0.127 mm on the surface of the main wing avoids the instability by creating a small gap for fluid. When the SMA SCF and wing are in contact in the structural model during slat articulation, the parts are separated in the fluid model by the small gap.
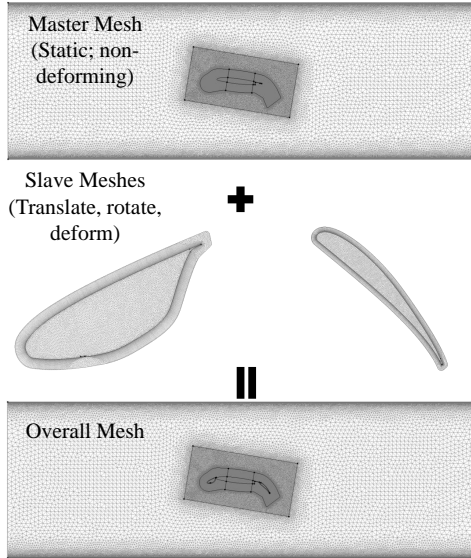
FIGURE 5. Overset mesh implementation for FSI analysis of the SCF-treated, deployed configuration.

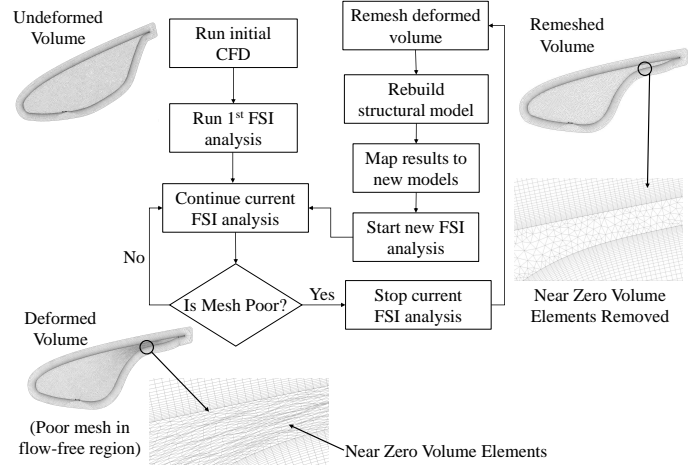**FIGURE 6**. Flowchart of FSI analysis with remeshing scheme.

4.2 FSI Framework And Remeshing Scheme

The Abaqus Co-Simulation Engine (CSE) is utilized in the coupling of the structure and fluid models for FSI analysis. The coupling is weak and easy to implement due to a built-in link in SC/Tetra to the CSE. Weak coupling allows the two programs to solve physical quantities separately and transmit necessary data at specified time increments, enabling the use of user functions in Abaqus to capture SMA behavior. Displacement of specified surfaces are transmitted from Abaqus to SC/Tetra while SC/Tetra provides the pressure loading. For this work, the outer mold line of the slat/SCF is the only surface linked between the two models.

During FSI analysis of slat/SCF articulation, the portion of the slave mesh representing the slat-cove is significantly reduced, resulting in the creation of zero volume elements. This led to the development of a slave mesh remeshing scheme. A flowchart of the scheme is shown in Fig. 6. At specified stages of the slat articulation, when the mesh is deemed poor, the FSI analysis is stopped and the slave mesh is rebuilt. Flow results from the final cycle of the previous FSI analysis are mapped as initial conditions to the new analysis. The remeshing process of the fluid model also requires rebuilding of the structural model to relink the structural and fluid models.

4.3 Fully Deployed SCF

FSI analysis is conducted on the SMA SCF with the slat in a fixed, fully deployed configuration at $6°$ and $8°$ angle of attack and with inlet speeds of $15\,\text{m/s}$ and $20\,\text{m/s}$ (and corresponding turbulence properties). Prior to each FSI analysis, CFD is con-

ducted to develop the flow to a near-steady condition, allowing for reduction of overall computational runtime. The analysis is conducted over $0.75\,\text{s}$ with a time step of $0.000025\,\text{s}$. Structural results are recorded every $0.005\,\text{s}$. Figure 7 shows the displacement time response of the node with the maximum deflection at the end of the analysis and contour plots of the displacement field for all four flow conditions. As seen in the figure, the maximum displacement occurs for all four cases generally in the same location in the aft third of the SCF. The SCF deflection shows a transient response at the start of the analysis but decays to a very small amplitude about a steady value as the fluid and structure reach a steady response. The displacement is virtually constant near the end of analysis for all flow conditions except the $6°$, $15\,\text{m/s}$, case which exhibits noticeable oscillatory behavior remaining. This indicates that there are flow conditions that may result in oscillation of the SCF and investigation is ongoing. At $15\,\text{m/s}$, the average maximum displacement for both angles is similar in value (approximately $0.04\,\text{mm}$). However, at the higher flow speed, the steady displacements for the two angles are further apart suggesting that the angle of attack may have an increasing effect on the SCF displacement as the flow speed is increased. Additionally, the 33% increase in flow speed (from 15 to $20\,\text{m/s}$) results in an approximate 75% increase in the maximum deflection. This is reasonable since the pressure acting on the SMA SCF is quadratically proportional to velocity.

4.4 Transient Retraction/Deployment

The other case considered for the FSI analysis is retraction and deployment of the SMA SCF with flow. This analysis is believed to be one of the first FSI analyses of an SMA-based morphing structure attached to a rigid body (the slat) that is moving relative to a fixed rigid body (the main wing) and exhibits significant volume change and contact between bodies. As with
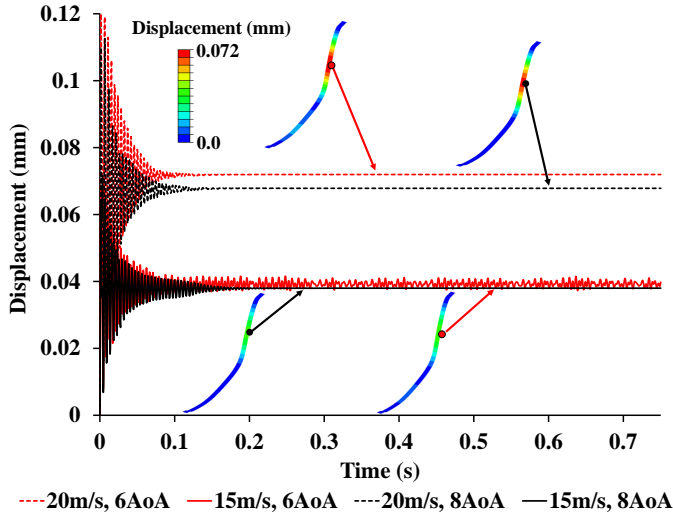
FIGURE 7. Displacement of SMA SCF during FSI analysis for the fixed fully deployed case. Contour plots are from the final time increment.

the fixed, fully deployed case, an initial CFD analysis is used to develop the flow for both the fully deployed and retracted configurations. Turbulence measurements in the test section had not been conducted at the time of the analysis. Instead, inlet conditions are assumed to be approximately laminar. Inlet velocity is set to 15 m/s and the wing is oriented at 8° angle of attack. During this analysis, the remeshing scheme of Fig. 6 is implemented to fully retract and deploy the SCF. For slat retraction, the SCF/slat slave mesh is remeshed at slat positions corresponding to 50% retraction and 90% retraction. For slat deployment, the SCF in the structural model is initially retracted into its stowed configuration separately from the fluid model to setup the slat/SCF slave mesh. During the deployment, remeshing occurs once at 85% deployment as the hinge is snapping into its deployed state. Note that a few fluid elements in the vicinity of the hinge are deleted to accommodate the redeployment of the hinge due to a localized, significant reduction of fluid volume as the hinge redeploys. Both retraction and deployment simulations are conducted over 0.5 s with a time step of 0.00005 s. Note that the articulation of the high-lift devices in the analysis (0.5 s) is much faster than the actual system in an aircraft (typically 20-30 s).

Figure 8 shows the velocity contours around the CRM wing at various stages of slat/flap articulation. The SMA SCF is able to fully stow into its retracted position and redeploy while under aerodynamic loading. The flow separation on the flap, particularly in the fully deployed, high-lift configuration, is mainly due to the low Reynolds number of the flow, i.e., low flow speed and small scale. As the high-lift devices are stowed, the overall magnitude of velocity across the surface of the wing (with the exception of the slat leading-edge) decreases due to the re-

duction in the camber of the wing and elimination of the suction peaks for the flap and main wing. Another interesting behavior, first observed in previous work [12], occurs when the SMA SCF is in contact with the main wing. Flow over the leading edge of the main wing is prevented, leading to flow separation off the slat/SCF and reattachment further downstream on the main wing. The behavior simulates a drooped leading edge, but the effect reduces as the high-lift devices near full stowage. The velocity contours return to the original distribution as the high-lift devices are redeployed. During deployment, the SMA SCF remains in contact with the main wing and in a stowed configuration simulating an alternative SMA-based aeroacoustic noise reduction system known as the slat-gap filler (SGF) [20]. The SCF configuration during most of the retraction cycle is significantly different than the SCF configuration during deployment at the same percent deployment, which could potentially affect the flow around the wing. This can be observed in Fig. 8 at 40% retracted and 60% deployed where the wing is at the same percent deployment. Overall the distribution of the velocity contour is fairly similar between the partially retracted and partially deployed configurations. The main differences are in the vicinity of the slat. The flow is slightly higher at the leading edge and extends further into the flow field away from the main wing for the 40% retracted configuration. Additionally, the 60% deployed configuration has a larger low velocity region between the slat and main wing due to the SCF being stowed. These differences in velocity contours for the two configurations may result in different global responses such as lift and drag of the wing.
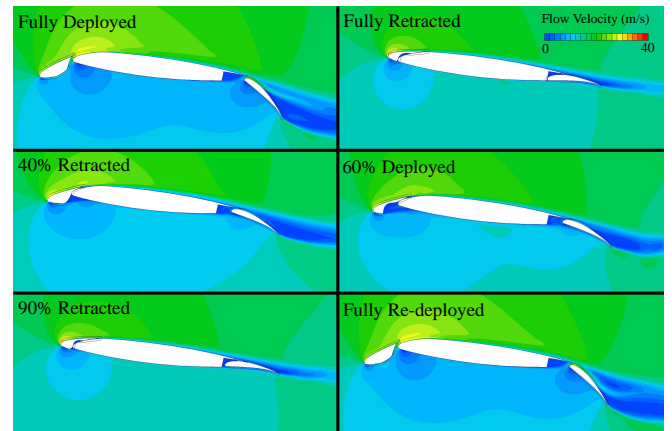
FIGURE 8. Velocity contours of CRM at various retraction and deployment stages of the high-lift devices.

The lift coefficient versus percent deployment for the FSI analysis is shown in Fig. 9 for both retraction and deployment phases of slat articulation. As expected, the lift decreases during retraction of the slat as the wing transitions from the high-lift
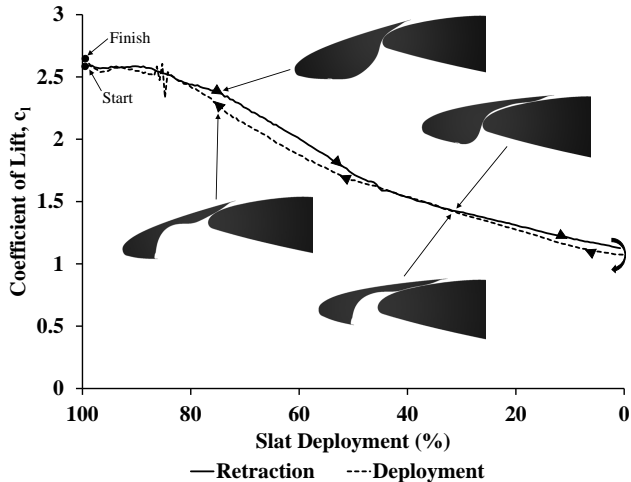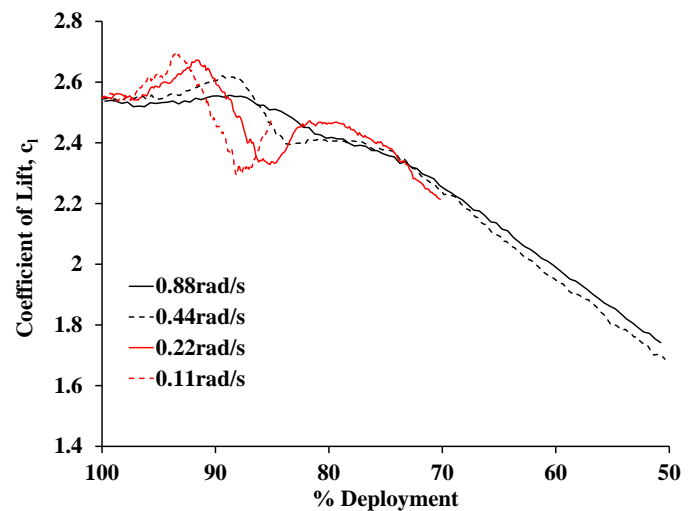
FIGURE 9. Lift coefficient of wing versus % deployment for retraction and deployment cycles.

to the cruise configuration and then increases as the high-lift devices are deployed. However, there are some differences in the predicted lift between the retraction and deployment phases of articulation. The discrepancies in lift at 0% and 100% deployment are unexpected and may be due to differences in the deformed and undeformed meshes in those configurations. The differences in lift between 50% and 80% deployment are at least partially attributable to physical differences in configuration. For example, the flow remains attached over a larger portion of the slat/SCF OML in the retraction phase and produces greater lift than the corresponding slat position in the deployment phase (see Fig. 8). The erratic fluctuation in lift during deployment at 85% is due to SCF/hinge redeployment, which is accompanied by oscillation of the SCF and a brief period of a variable, small gap between the SCF and main wing. Flow through that small, variable gap produces fluctuations in the boundary layer on the top of the wing that commensurately affect the lift production.

The effect of the retraction rate is also studied by reducing the rate of retraction for the slat and flap. Figure 10 shows lift versus percent deployment for four retraction rates. The same FSI model is used for each case with a time step of 0.00005 s. Note that the 0.88 rad/s retraction rate case requires 0.5 s to achieve full retraction and corresponds to results shown in Fig. 9. Only partial retraction[1] is considered due to the computational runtime required to conduct full retraction for slower cases. Simply reducing the retraction rate by a factor of two (0.88 rad/s) changes the lift-deployment curve compared to the original 0.88 rad/s case. Between fully deployed and 88% deployment, the lift increases for the 0.44 rad/s case while the 0.88 rad/s case exhibits a fairly constant lift. Additionally for

the 0.44 rad/s case, lift decreases between 88% and 84% deployment, then is constant until approximately 78% deployment where it follows a similar path as the 0.88 rad/s case. Past 70% deployment, the lift for the 0.44 rad/s retraction rate case is between the lift for the 0.88 rad/s retraction/deployment cycles of Fig. 9. Decreasing the retraction rate further to 0.22 rad/s and 0.11 rad/s results in the increase in lift (which grows with decreased retraction rate) followed by the rapid decrease in lift (between 88% and 84% deployment for the 0.44 rad/s case) occurring sooner in the retraction cycle. Additionally, both the 0.22 rad/s and 0.11 rad/s cases exhibit an increase in lift following the significant drop. These results suggests that a phenomena is not captured at fast retraction rates and may resolve some of the discrepancies discussed for Fig. 9. Examination of the velocity contour plot between 5% and 15% deployment, where the SCF comes into contact with the main wing (occurs at 14%), shows that a jet of high speed flow is created as the distance between the SCF and the main wing decreases. This jet appears to initially increase the lift, but soon results in separation of flow over the surface of the main wing and thus decreases the lift.

FIGURE 10. Lift coefficient of wing versus % deployment for different retraction rates.

5 Experimental Model Results and Comparisons

This section details work with the experimental model. A description of the wind tunnel model is provided followed by a discussion of structural and aerodynamic results that are compared to computational data.

---

[1]The 0.44 rad/s, 0.22 rad/s, and 0.11 rad/s are retracted to 50%, 30%, and 15% deployment, respectively.

5.1 Wind Tunnel Model Description

The wind tunnel model (see Fig. 11) is 1.22 m in span with a stowed chord of 0.32 m, and is comprised of an aluminum spar for main structural support and 3D-printed ABS plastic shells mounted to the spar for the wing outer mold line. The slat and flap are also constructed of 3D-printed ABS plastic by additive manufacturing, but the parts are solid (as opposed to shells) and are stiffened by integral steel rods, as seen in Fig. 12(a). Even with the stiffeners, the slat and flap lacked the stiffness required to span the 1.22 m test section without additional support at the midspan. It is for this reason that a steel guide track is introduced at the midspan of the model in addition to tracks at the side walls for support and guidance of the slat and flap during articulation of the high-lift system. Linear actuators, mounted to the spar, control the position of the slat and flap along the guide tracks at the midspan and sides of the model, allowing for the evaluation of multiple configurations. Two variants of the 3D printed slat are discussed in this work: 1) the untreated slat taken from the CRM geometry and 2) a slat modified to include the deformable SMA SCF. The modified slat has a steel trailing-edge piece for improved bonding of the SMA SCF and a steel cusp. The wing is mounted to load cells (for lift and drag measurements) in a test section for the Texas A&M University 3 ft-by-4 ft closed loop tunnel. Angle of attack of the model is controlled using a pitch-plunge gear system on the test section.
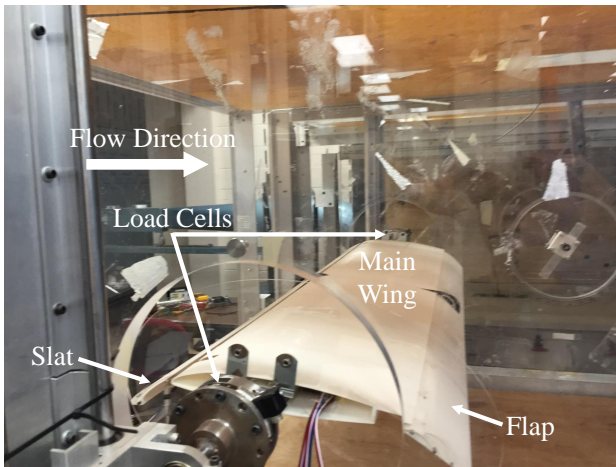
FIGURE 11. Physical wind tunnel model of CRM wing 2D section (from [11]).

The SCF (see Fig. 12(a)) is manufactured using 16.5 cm-18 cm spanwise sections of 0.0762 mm (0.003 in) thick superelastic SMA sheet that are shape set into the SCF profile (see Fig. 5.1 and reference [12] for additional detail). The SCF sections are then bonded with epoxy to the modified slat. Aluminum


(a) Physical SCF

(b) Computational SCF
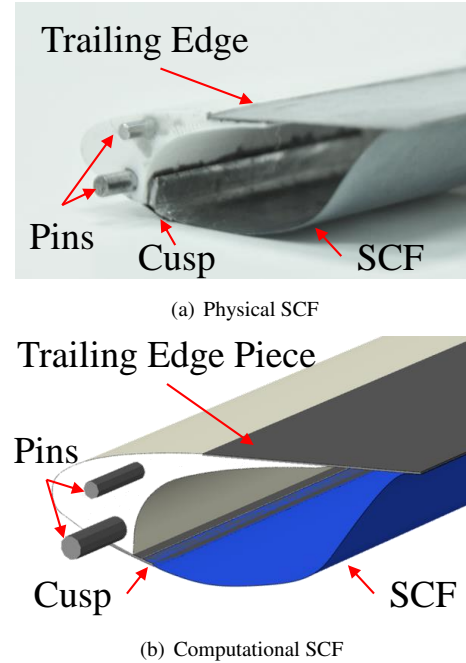
FIGURE 12. Computational and physical SCF-treated slat with attached SCF.

tape is used as a hinge at the slat cusp to allow the SMA SCF to freely rotate, accommodating SCF retraction and deployment. Figure 13 shows the retraction and deployment cycle of the physical SMA SCF. Starting from the fully deployed position (**1**), the linear actuators retract the slat, deforming the SCF around the main wing (**2**-**3**) into its retracted configuration where the SCF is stowed between the slat and main wing (**4**). As the slat is redeployed (**5**), the SCF loses contact with the main wing and returns to its original configuration.

There are manufacturing imperfections, such as bending of the slat at high levels of retraction, that may lead to modeling discrepancies. To provide a means of initial structural comparisons, a full-span, 3D version of the computational model is developed (see Fig. 12(b)). In this model, the slat is modeled as a deformable body with material properties of 3D-printed plastic and steel. The deformable slat is tied to pins in order to simulate the boundary conditions of the wind tunnel model.

The position and shape of the SCF in the wind tunnel model is tracked using two systems: 1) a rotating laser measurement sensor, and 2) a digital image correlation (DIC). Both systems are positioned underneath the test section to view a quarter-span section of the SCF through a transparent plexiglass portion of the test section floor. The laser sensor is able to give accurate distance readings between a point on the model and the sensor. Mounting the laser sensor to a rotating rod with an attached potentiometer allows for scanning of the model shape, which was
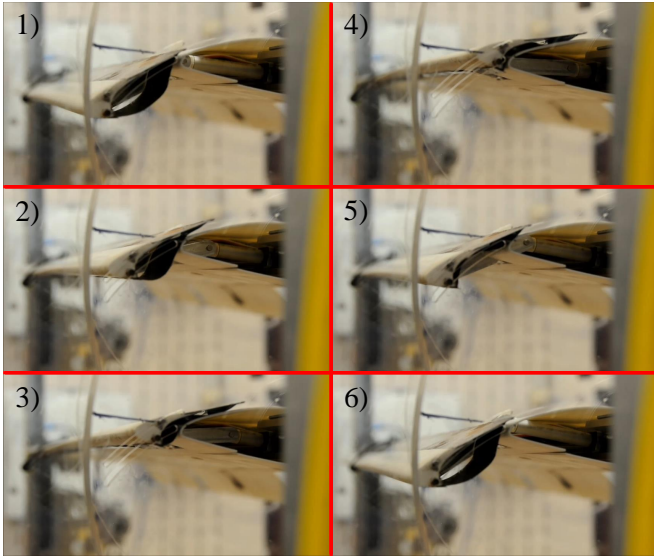
FIGURE 13. Retraction and deployment of wind tunnel model slat/SCF: 1) fully deployed, 2) SCF deforming around main wing, 3) hinge clearing leading-edge, 4) retracted SCF, 5) partial redeployment, 6) full redeployment.

the OML of the SCF for this work. The distance and rotation measurements can then be converted into Cartesian coordinates. This system is limited to 2D sweeps of the model. DIC is an optical technique that uses two offset cameras to take 3D images of a structure treated with a painted speckle pattern. With specialized DIC software, points in the speckle pattern are tracked and used to determine the displacement of structure from an original reference image. In this work, the reference image is of the SCF in a fixed, fully-deployed configuration under no aerodynamic loading (i.e., no flow through test section). Note that as the SCF is stowed, the speckle pattern will become progressively hidden by the main wing.

Due to the bending of the plastic slat during retraction (and at high speeds and angles of attack due to high aero-loads), a stainless steel slat is manufactured to replace the plastic slat. Note that the steel trailing edge and cusp are epoxied to the steel slat in a similar manner to the plastic slat due to manufacturing constraints. The geometry of the steel slat is the same as the modified (for the SCF) 3D-printed plastic slat with a slightly deeper cove to better accommodate stowage of the SCF. Additionally, the steel slat is 1.22 m long, which allows removal of the center guide track for the slat. Removal of the center guide track and the reduction in bending of the slat under aerodynamic loading is expected to result in more uniform flow over the wing in the spanwise direction. An SMA SCF will be added to the steel slat in future work.

5.2   Preliminary Wind Tunnel Results

Preliminary wind tunnel testing of the physical model with the untreated steel slat is conducted for both the retracted and fully deployed configurations with a freestream velocity of approximately 15 m/s in the Texas A&M University 3 ft-by-4 ft closed loop tunnel. Lift versus angle of attack curves for both computational[2] and preliminary experimental results are shown in Fig. 14. The predicted and measured lift compare favorably over the range of the experiments and both show the expected, near-linear increase in lift with angle of attack from -2° to 8°. At angles above 8°, the lift levels off potentially indicating that the wing is approaching stall.

Experimental results indicate a slightly lower zero-lift angle of attack (-2.5°) than the computational data (-2°). Discrepancies between results may be due to 3D flow effects generated by geometric features not modeled in the computational analysis including the side walls, guide tracks, and actuators.
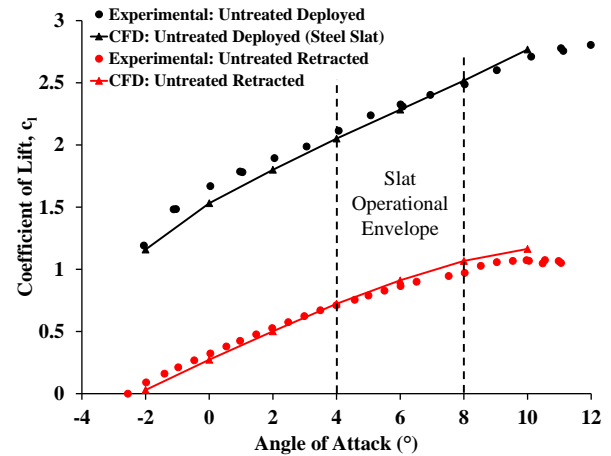
FIGURE 14. Computational and experimental results of CRM wing in deployed and retracted configurations.

Compared to the retracted configuration, the predicted and measured lift for the deployed configurations show the expected increased lift due to the increase in camber and wing area. Though not shown, the CFD results for the untreated deployed model based on the 3D-printed plastic slat (shallow cove and no steel pieces) and the SCF-treated deployed model are approximately equal to the shown computational data for the steel slat geometry. This indicates that computationally, neither the new slat geometry, which has a deeper cove and steel cusp/trailing edge, or addition of the SCF significantly affects the lift. Both computational and experimental data exhibit a near-linear lift variation from 0° to 10° (12° for experimental) and a similar

---

[2]Geometry of the untreated retracted CFD model is based on the plastic slat.

roll-off in lift below 0° angle of attack, similar to the response observed in previous work [11]. It is expected that a further decrease in angle of attack will lead to a significant nonlinear decrease in lift due to massive separation. Predicted and measured lift compare best between 4° and 10°, which encompasses the typical operational envelop (4° to 8°) of the deployed high-lift system. There are some differences between the predicted and measured results that are likely attributable to the 3D flow effects mentioned for the retracted configuration and turbulence model fidelity. The flow field around the deployed configuration is sensitive to the inlet properties so more turbulence measurements may improve modeling of the flow. Overall, the computational models (both retracted and deployed) are fairly accurate in predicting the lift of the experimental model providing some validation of the computational tools used in FSI analysis. Further wind tunnel testing at other inlet velocities and with the addition of pressure measurements will provide more means of comparing computational and experimental models.

5.3 Structural Measurements of SCF Deformation

Laser sensor and DIC measurements of the SCF are taken at approximate 10% increments of slat articulation. Due to limited space underneath the test section, laser sensor and DIC measurements are taken during separate tests. Additionally, the model is not subjected to aerodynamic loading while SCF deformation is measured. A no-flow condition is considered due to: 1) an electromagnetic field generated by the pitch-plunge system (unneeded under no flow) that affects the unshielded potentiometer, and 2) potential rigid body movement of the slat when aerodynamically loaded, due to high manufacturing tolerances, which make comparisons between the DIC and laser systems (and computational tools) more difficult.

Figure 15 shows the position and shape of the SCF at various stages of slat retraction/deployment using both measurement systems[3] overlaid onto results from the computational-structural model of the wind tunnel slat/SCF. During early stages of retraction, the experimental and computational data show good agreement. However, as the slat retracts further than 50% (but prior to the SCF snapping into a stowed configuration), the computational and experimental results diverge. This is attributed to the high loading from contact between the main wing and SCF acting on the actuators, which offers the slat mobility in the physical model to deflect away from the main wing. This geometric inaccuracy delays SCF retraction in the physical model and is not captured in the computations. Furthermore, there is a sharp change of geometry in the vicinity of the contact area that may disrupt laser measurements. Once the SCF snaps into a stowed configuration and during the deployment cycle, when contact force is assisting the actuators, the experimental and computa-

---

[3]DIC data is extracted from a slice of the 3D results in the same location where measurements with the laser sensor are taken.
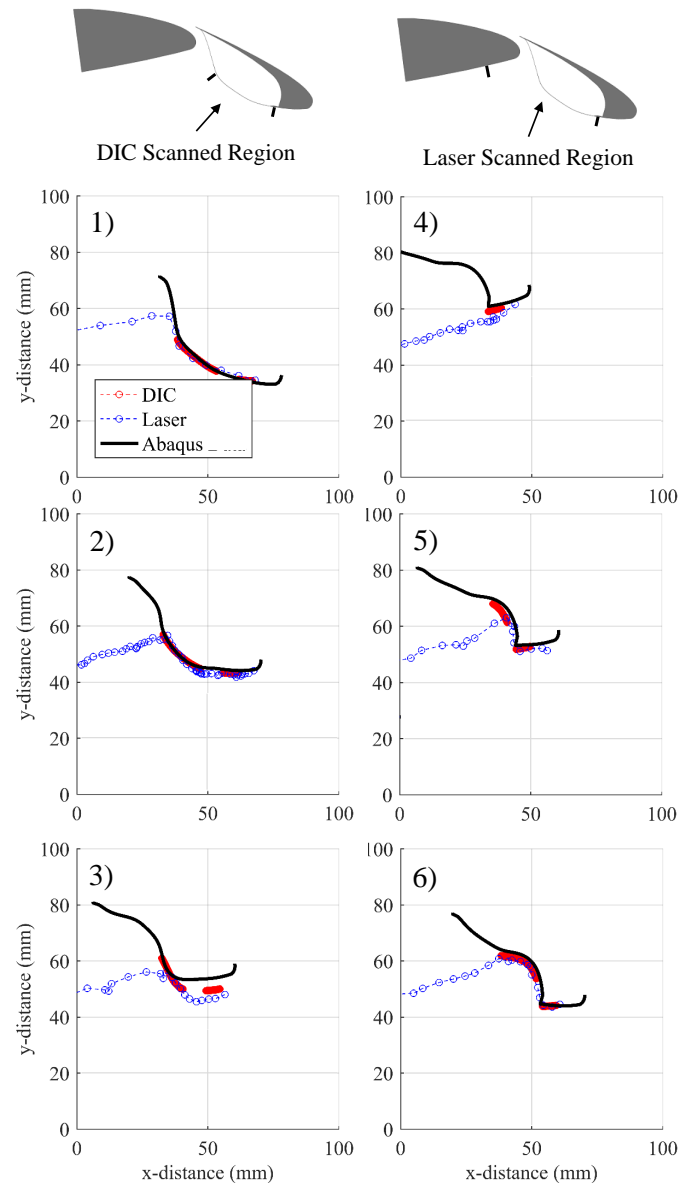
FIGURE 15. Retraction and deployment of wind tunnel model slat/SCF: 1) fully deployed, 2) SCF deforming around main wing, 3) hinge clearing leading-edge, 4) retracted SCF, 5) partial redeployment, 6) full redeployment.

tional results match quite well again. Overall, the computational results match the DIC measurements better than laser sensor measurements. This is not surprising since the laser sensor is a low resolution tool compared to DIC. However, the laser sensor does provide a wider field of view and does not require a distributed surface treatment. These results validate the computational structural model, which can be used in future work to

understand how the wind tunnel model SCF behaves during retraction and deployment.

6 Summary and Conclusions

The goal of this work was to improve upon past computational and experimental efforts that focused on understanding how the SMA SCF behaved in flow. Both computational and experimental models were based on a scaled, high-lift variant of the Boeing-NASA CRM. Using recently obtained measurements of turbulent flow properties, flow through the test section was modeled more accurately. FSI analysis of the SMA SCF considered two load cases: 1) fixed and fully deployed, and 2) slat retraction/deployment. For the fixed, fully deployed case, FSI analysis was conducted at two speeds and two angles of attack. The maximum displacement of the SCF was similar for the two angles at the same flow speed, but higher flow speeds may lead to more sensitivity of the displacement to the angle. In addition, the SCF demonstrated small oscillatory behavior at the $6°$ angle of attack in 15 m/s flow. Using an improved FSI model and a newly developed remeshing scheme, full retraction and deployment simulations of the SCF were achieved. These results are believed to be one of the first FSI analyses of an SMA morphing structure moving relative to a fixed body and exhibiting significant volume changes and contact between multiple bodies. Lift coefficient versus percent slat deployment during both deployment and retraction cycles showed significant differences between 80% and 50% deployment. It is believed that the lift discrepancy is due to configuration differences that affect the lift production.

A steel slat was manufactured and installed in the wind tunnel model, replacing the less-stiff plastic slat and allowing removal of a midspan support for the slat, to reduce undesirable flow effects associated with the original model. Preliminary wind tunnel tests were conducted with the improved model with the new slat in both retracted and deployed configurations. Experimental and computational lift-AoA curves compared favorably for both configurations. A DIC system and laser displacement sensor were used to measure the position and shape of the SCF on the plastic slat as it was retracted and deployed. Both measurement systems were then compared to a structural model of the slat/SCF. Through early stages of retraction and most of the deployment, computational and experimental results align quite well. At high levels of retraction, the results diverged likely due to the high contact loading between the slat and SCF forcing geometric inaccuracy in the physical model that delays SCF stowage.

Future work will continue FSI analysis of the SMA SCF. Refinement of the remeshing scheme will improve runtime efficiency during retraction/deployment. Further turbulence measurements will improve modeling of the flow through the test section. A thinner SMA SCF will be integrated with the steel slat for the purpose of observing larger aeroelastic responses in both the computational and physical models at the flow speeds of the wind tunnel. Additionally, the thinner SMA SCF will reduce the loading on both the actuators and slat, improving position control and limiting rigid body displacements currently not captured in the computational FSI model. Finally, an acoustically treated test section will be developed, allowing for noise measurements of models with and without an SMA SCF.

REFERENCES

[1] Gleine, W., Mau, K., and Carl, U., 2002. Aerodynamic noise reducing structure for aircraft wing slats. U.S. Patent 6,394,396.

[2] Streett, C., Casper, J., Lockard, D., Khorrami, M., Stoker, R., Elkoby, R., Wenneman, M., and Underbrink, J., 2006. "Aerodynamic noise reduction for high-lift devices on a swept wing model". *44th AIAA Aerosciences Meeting and Exhibit*(AIAA Paper 2006-212).

[3] Horne, W., James, K., Arledge, T., Soderman, P., Burnside, N., and Jaeger, S., 2005. "Measurments of 26%-scale 777 airframe noise in the NASA Ames 40-by 80 Foot Wind Tunnel". *11th AIAA/CEAS Aeroacoustics Conference*(AIAA Paper 2005-2810).

[4] Imamura, T., Ura, H., Yokokawa, Y., Enomoto, S., Yamamoto, K., and Hirai, T., 2007. "Designing of slat cove filler as a noise reduction device for leading-edge slat". *13th AIAA/CEAS Aeroacoustics Conference*(AIAA Paper 2007-3473).

[5] Hartl, D. J., and Lagoudas, D., 2007. "Aerospace applications of shape memory alloys". *Proceedings of the Institution of Mechanical Engineers, Part G: Journal of Aerospace Engineering,* ***221 (Special Issue)***, pp. 535–552.

[6] Turner, T., Kidd, R., Hartl, D., and Scholten, W., 2013. "Development of a sma-based, slat-cove filler for reduction of aeroacoustic noise associated with transport-class aircraft wings". *Proceedings of the ASME 2013 Conference on Smart Materials, Adaptive Structures and Intelligent Systems*(SMASIS2013-3100).

[7] Scholten, W., Hartl, D., and Turner, T., 2013. "Analysis-driven design optimization of a sma-based slat-cove filler for aeroacoustic noise reduction". *Proceedings of the ASME 2013 Conference on Smart Materials, Adaptive Structures and Intelligent Systems*(SMASIS2013-3104).

[8] Scholten, W., Hartl, D., Turner, T., and Kidd, R., 2016. "Development and analysis-driven optimization of a superelastic slat-cove filler for airframe noise reduction". *AIAA*, **54**(3), pp. 1078–1094.

[9] Scholten, W., Hartl, D., Strganac, T., and Turner, T., 2015. "Reduction of actuation loads in a self-deploying sma-based slat-cove filler for a transport aircraft". *Proceedings of the ASME 2015 Conference on Smart Materials, Adaptive Structures and Intelligent Systems*(SMASIS2015-9015).

[10] Arena, G., Scholten, W., Rainer, G., Pirrera, A., Hartl, D., and Turner, T., 2018. "A tailored nonlinear slat-cove filler for airframe noise reduction". *Proceedings of the ASME 2018 Conference on Smart Materials, Adaptive Structures and Intelligent Systems*(SMASIS2018-8079).

[11] Scholten, W., Patterson, R., Volpi, J., Hartl, D., Strganac, T., and Turner, T., 2016. "Noise reduction in a high lift wing using smas: Computational fluid-structural analysis". *Proceedings of the ASME 2016 Conference on Smart Materials, Adaptive Structures and Intelligent Systems*(SMASIS2016-9196).

[12] Scholten, W., Patterson, R., Chapelon, Q., Hartl, D., Strganac, T., and Turner, T., 2017. "Computational and experimental fluid-structure interaction assessment of a high-lift wing with a slat-cove filler for noise reduction". *AIAA SciTech*.

[13] Lacy, D., and Sclafani, A., 2016. "Development of the high lift common research model (hl-crm): A representative high lift configuration for transonic transports". *54th AIAA Aerospace Sciences Meeting*(AIAA 2016-0308).

[14] Vassberg, J., DeHann, M., Rivers, S., and Wahls, R., 2008. "Development of a common research model for applied cfd validation studies". *AIAA paper*, **6919**.

[15] Abaqus, 2011. *Analysis User's Manual*. Dassault Systèmes of America Corp., Woodlands Hills, CA.

[16] Qidwai, M., Hartl, D., and Lagoudas, D., 2008. "Numerical implementation of an sma thermomechanical constitutive model using return mapping algorithms". In *Shape Memory Alloys: Modeling and Engineering Applications*, D. Lagoudas, ed. Springer-Verlag, New York, ch. 4, pp. 189–231.

[17] ASTM, 2016. *Standard Test Methods of Tension Testing of Metallic Foil*. ASTM International.

[18] SC/Tetra, 2015. *User's Guide*. Software Cradle Co., Ltd.

[19] Menter, F., 1993. "Zonal two equation k-ω turbulence models for aerodynamic flows". *AIAA*(AIAA 1993-2906).

[20] Turner, F., and Long, D., 2015. "Development of a sma-based, slat-gap filler for airframe noise reduction". *AIAA*(AIAA 2015-0730).